Smart Structures and Systems, *Vol. 36. No. 4 (2025) 223-237*
https://doi.org/10.12989/sss.2025.36.4.223

Smart vibro-acoustic control of FGP concrete structures via NC shunt damping and DNN-GA optimization

Bin Wang [1], Bo Han*[2], Mehran Safarpour**[3] and Murat Yaylacı [4,5]

[1] *School of Civil Engineering and Transportation Engineering, Yellow River Conservancy Technical University, Kaifeng 475004, Henan, China*
[2] *College of Science, Xi'an University of Architecture and Technology, Xi'an 710311, Shanxi Province, China*
[3] *Faculty of Engineering, Department of Mechanics, Tarbiat Modares University, Tehran, Iran*
[4] *Department of Civil Engineering, Recep Tayyip Erdogan University, 53100, Rize, Turkey*
[5] *Turgut Kiran Maritime Faculty, Recep Tayyip Erdogan University, 53900, Rize, Turkey*

(*Received July 21, 2025, Revised September 27, 2025, Accepted November 25, 2025*)

Abstract. This research introduces a smart control paradigm for the stochastic vibro-acoustic suppression of functionally graded piezoelectric (FGP) concrete plates, which are developed for the smart concrete structures and systems domain. The proposed method integrates negative capacitance piezoelectric shunt damping (NCPSD), the Carrera Unified Formulation (CUF), and a smart hybrid optimization mechanism comprising deep neural networks and Genetic algorithms (DNN-GA). A detailed multi-layer modeling framework is created through CUF, which efficiently depicts the complex electromechanical responses such as shear deformation, geometric nonlinearity, and spatial grading in the piezoelectric properties. A smart passive-active damping interface is realized by embedding piezoelectric sensor-actuator pairs connected to a negative capacitance-resistive-inductive (NC-RL) shunt circuit. This setup significantly boosts dynamic adaptability and provides broad bandwidth attenuation. The DNN-GA architecture controls the parameters by tuning them adaptively according to the stochastic excitations and thus navigating through the complex nonlinear response space of the FGP concrete system effectively. The genetic algorithm proceeds rapidly through the zones of the optimal solutions while the deep neural network ensures real-time prediction and adaptation amid the parametric uncertainties. There was a considerable reduction in structural vibration and radiation of acoustic energy particularly in the mid-to-high frequency range, as simulation results indicated. This research supports the possibility of using smart damping solutions for smart concrete structures and systems abroad, especially in the aerospace and automotive industries where the ability to reduce noise and vibrations adaptively is needed the most.

Keywords: DNN-GA algorithm; intelligent structural dynamics; functionally graded piezoelectric concrete plates; negative capacitance shunt damping; smart concrete structures and systems; stochastic vibro-acoustic control

1. Introduction

Piezoelectric materials play a pivotal role in modern engineering applications due to their unique ability to convert mechanical energy into electrical energy and vice versa (Gupta *et al*. 2023, Chen *et al*. 2025). These materials are essential in developing smart structures that can actively respond to external stimuli (Long *et al*. 2024). Their dual sensing and actuation capabilities make them highly suitable for vibration control, structural health monitoring, and energy harvesting systems (Zhang *et al*. 2024). The integration of piezoelectric materials into composite structures enhances their multifunctional performance without significantly increasing weight (Najd *et al*. 2024). In aerospace and automotive industries, they contribute to noise reduction, active damping, and adaptive surface morphing (Sha *et al*. 2024). Moreover, their application in biomedical devices, such as ultrasonic sensors and actuators, has significantly advanced diagnostic and therapeutic technologies (Ravanbod and Ebrahimi-Nejad 2024). Advances in functionally graded piezoelectric materials (FGPMs) allow for spatial tailoring of properties, optimizing performance under varying operational conditions (Gao *et al*. 2025). The combination of piezoelectricity with intelligent control algorithms enables real-time adaptively and resilience against uncertainties (Kurt *et al*. 2024). Overall, piezoelectric materials serve as a cornerstone in the design of next-generation smart, adaptive, and sustainable engineering systems.

Sound radiation characteristics are critical for understanding how structures emit acoustic energy into their surrounding environment (Reddy *et al*. 2024). These characteristics directly influence noise levels, which are essential in applications where acoustic performance and comfort are important, such as in aerospace, automotive, and building acoustics (Patil and Pitchaimani 2024). Controlling sound radiation helps in reducing noise pollution and enhancing the stealth or efficiency of mechanical systems (Liu *et al*. 2024). The study of structural-acoustic coupling provides insight into how vibrations translate into airborne noise, enabling targeted

*Corresponding author, Ph.D.,
E-mail: 1735616138@qq.com
**Co-corresponding author, Ph.D.,
E-mail: m_safarpour@modares.ac.ir

ISSN: 1738-1584 (Print), 1738-1991 (Online)

design improvements (Li *et al*. 2024). Ultimately, optimizing sound radiation behavior contributes to the development of quieter, safer, and more efficient engineering systems (Wei *et al*. 2024).

The CUF is a powerful and versatile modeling framework for analyzing structures with complex geometries and material behaviors (Carrera 1995). CUF enables the derivation of refined structural theories from a unified mathematical base, accommodating various kinematic assumptions without the need for ad hoc formulations (Carrera 1998). It allows for the systematic development of beam, plate, and shell models by expanding the unknown variables over the cross-section using generalized functions (Carrera 2001). One of CUF's primary advantages lies in its hierarchical nature, which ensures enhanced accuracy through higher-order theories while maintaining computational efficiency (Carrera 2003). This formulation supports both linear and nonlinear analyses, making it suitable for advanced structural applications under diverse loading and boundary conditions (Carrera and Kröplin 1997). CUF is particularly effective in modeling multilayered and functionally graded materials, where variations in properties across the thickness must be accurately captured (Carrera 2005). Its compatibility with finite element methods facilitates the implementation of sophisticated element types and coupling with other physical fields (Robaldo *et al*. 2006a). CUF has been successfully applied in aeroelasticity, smart structures, and nano-engineered systems, demonstrating its adaptability across scales (Carrera and Pagani 2014). Moreover, it enables unified treatment of mechanical, thermal, and electromechanical problems within a consistent mathematical structure (Carrera and Zozulya 2024). Overall, CUF provides a comprehensive and expandable framework for the next generation of high-fidelity structural analyses in engineering science (Robaldo *et al*. 2006b).

Stability analysis is fundamental in engineering design, ensuring that structures can maintain equilibrium under various loading conditions without experiencing sudden failure (Fourn *et al*. 2018). It helps identify critical loads at which a structure may buckle or collapse, allowing for the safe and efficient design of load-bearing systems (Quan and Dinh Duc 2016). In aerospace, civil, and mechanical engineering, stability assessments are crucial for structures subjected to compressive forces, such as columns, panels, and shells (Eyvazian *et al*. 2022). Understanding post-buckling behavior through stability analysis enables engineers to exploit structural resilience without exceeding safety limits (Ebrahimi *et al*. 2017). This analysis is particularly important for slender and lightweight structures, which are more susceptible to instability (Guo *et al*. 2022). Advanced stability techniques account for geometric nonlinearities, material anisotropy, and varying boundary conditions, reflecting real-world complexities (Ebrahimi *et al*. 2016). Stability analysis also plays a significant role in the optimization of structures, ensuring performance under minimum weight or material usage (Yang *et al*. 2024). In dynamic environments, such as seismic or aerodynamic loading, stability criteria guide the design of systems that can withstand time-dependent disturbances (Moradi-Dastjerdi and Behdinan 2021). For smart and adaptive materials, including piezoelectric and functionally graded composites, stability studies help evaluate control strategies under mechanical and electromechanical loads (Fourn *et al*. 2018b). Overall, stability analysis ensures the structural integrity, reliability, and longevity of engineering systems across a wide range of applications (Al-Osta 2022).

This study introduces a novel and intelligent framework for suppressing stochastic vibro-acoustic responses in FGP plates by integrating NCPSD, the CUF, and a DNN-GA hybrid model. Leveraging the tunable electromechanical properties of FGP materials and the broadband damping characteristics induced by negative capacitance feedback circuits, the proposed approach enhances the concrete system's adaptability and energy dissipation efficiency under random excitations. CUF serves as a refined structural modeling platform that accurately captures the complex coupled mechanical-acoustic-piezoelectric behavior, including transverse shear deformation, multilayer interactions, and geometric nonlinearities, without relying on oversimplified assumptions of conventional plate theories. To adaptively control dynamic responses, distributed piezoelectric sensor-actuator networks are connected to optimized RL-NC shunt circuits, whose parameters are fine-tuned through the DNN-GA algorithm. The genetic algorithm explores the global hyperparameter space, while the deep neural network is trained to approximate the nonlinear dynamic behavior and predict concrete system performance under varying stochastic conditions. Stochastic analysis reveals that the optimized control system significantly suppresses both structural vibrations and acoustic radiation, particularly in mid- and high-frequency domains. The DNN-GA-enhanced design not only validates the theoretical model but also ensures robustness and adaptability under uncertainty, offering real-time responsiveness to fluctuating environmental and operational conditions. This intelligent, data-driven integration of CUF, NCPSD, and DNN-GA establishes a scalable, high-performance control architecture suitable for next-generation smart structures in aerospace, automotive, and precision engineering fields, where noise mitigation, structural integrity, and operational reliability are critical design goals.

2. The present problem model

Fig. 1 depicts a functionally graded piezoelectric plate with surface-mounted electrodes on both faces, designed with dimensions a (length), b (width), and h (thickness), and operating under random external loads while integrated with a shunt damping circuit.

When a voltage V_0 is applied across the electrodes, the FGP plate experiences an electric potential Φ. As shown in Table 1, the structure is made from a combination of two different piezoelectric materials.

Also, the properties of concrete are presented in Ref. (Zhao *et al*. 2024).

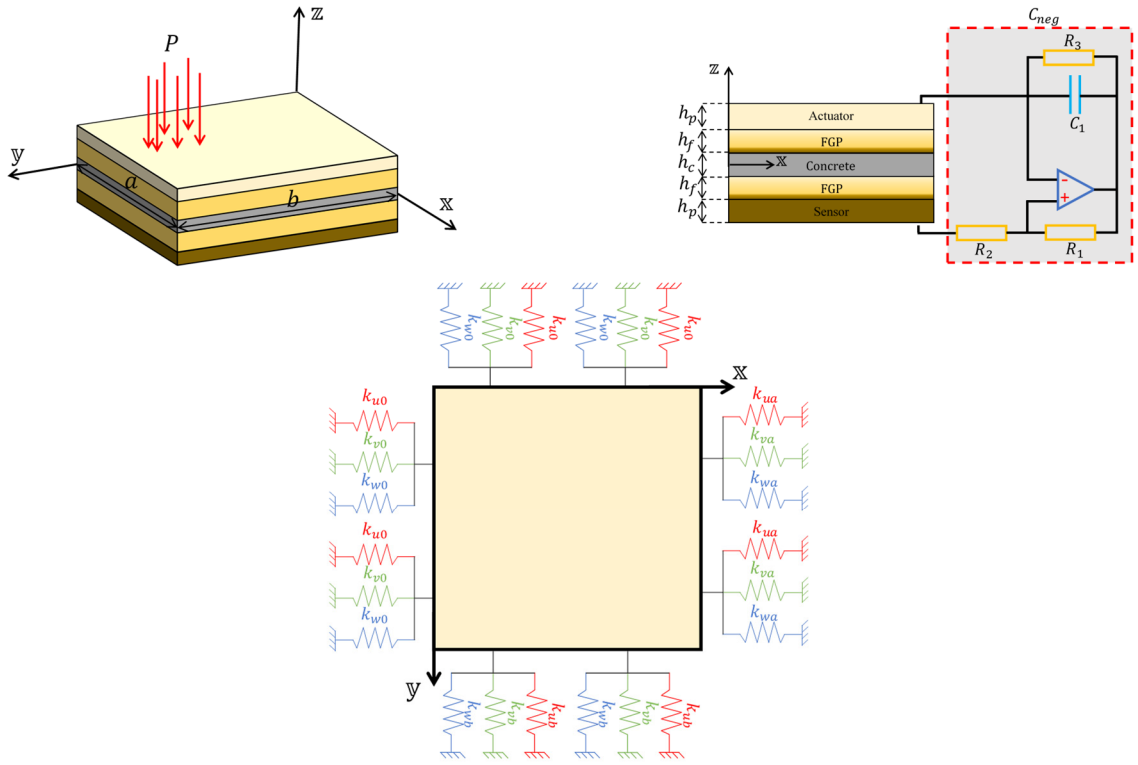

Fig. 1 The geometry and coordinate concrete systems of the smart concrete plate subjected to stochastic excitations with a piezoelectric shunt damping circuit

Table 1 Material properties (Vel *et al*. 2004, Ramirez *et al*. 2006, Yang 2010, Bodaghi and Shakeri 2012)

Properties	PZT-4 (Vel *et al*. 2004, Ramirez *et al*. 2006)	PZT-5H (Yang 2010, Bodaghi and Shakeri 2012)
$\mathbb{c}_{11} = \mathbb{c}_{22}\ (GPa)$	138.499	126
$\mathbb{c}_{12}\ (GPa)$	77.371	79.1
$\mathbb{c}_{13}\ (GPa)$	73.643	83.9
$\mathbb{c}_{33}\ (GPa)$	114.745	117
$\mathbb{c}_{55}\ (GPa)$	25.6	23
$\mathbb{c}_{66}\ (GPa)$	30.6	23.5
$\mathbb{e}_{31}\ \left(\frac{C}{m^2}\right)$	−5.2	−6.5
$\mathbb{e}_{33}\ \left(\frac{C}{m^2}\right)$	15.08	23.3
$\mathbb{e}_{15}\ \left(\frac{C}{m^2}\right)$	12.72	17
$\Xi_{11}\ \left(\frac{C^2}{m^2N}\right)$	1.306×10^{-9}	15.05×10^{-9}
$\Xi_{33}\ \left(\frac{C^2}{m^2N}\right)$	1.115×10^{-9}	13.02×10^{-9}
$\rho\left(\frac{kg}{m^3}\right)$	7600	7500

2.1 Material properties

The properties of the sandwich plate through its thickness, following an Eq. (1).

$$
\begin{aligned}
&\text{For:}\quad -\frac{h_c}{2}-h_f-h_p<\mathbb{z}<-\frac{h_c}{2}-h_f\\
&\quad \mathbb{c}_{ij}(\mathbb{z})=\mathbb{c}_{ij}^{b},\\
&\quad \mathbb{e}_{ij}(\mathbb{z})=\mathbb{e}_{ij}^{b},\\
&\quad \Xi_{ij}(\mathbb{z})=\Xi_{ij}^{b},\\
&\quad \rho(\mathbb{z})=\rho^{b}.\\
&\text{For:}\quad -\frac{h_c}{2}-h_f<\mathbb{z}<-\frac{h_c}{2}\\
&\quad \mathbb{c}_{ij}(\mathbb{z})=\mathbb{c}_{ij}^{u}\left(1-e^{\alpha\left(\frac{-2\mathbb{z}+h_c}{2h_f}\right)}\right)+\mathbb{c}_{ij}^{b}e^{\alpha\left(\frac{-2\mathbb{z}+h_c}{2h_f}\right)},\\
&\quad \mathbb{e}_{ij}(\mathbb{z})=\mathbb{e}_{ij}^{u}\left(1-e^{\alpha\left(\frac{-2\mathbb{z}+h_c}{2h_f}\right)}\right)+\mathbb{e}_{ij}^{b}e^{\alpha\left(\frac{-2\mathbb{z}+h_c}{2h_f}\right)},\\
&\quad \Xi_{ij}(\mathbb{z})=\Xi_{ij}^{u}\left(1-e^{\alpha\left(\frac{-2\mathbb{z}+h_c}{2h_f}\right)}\right)+\Xi_{ij}^{b}e^{\alpha\left(\frac{-2\mathbb{z}+h_c}{2h_f}\right)},\\
&\quad \rho(\mathbb{z})=\rho^{u}\left(1-e^{\alpha\left(\frac{-2\mathbb{z}+h_c}{2h_f}\right)}\right)+\rho^{b}e^{\alpha\left(\frac{-2\mathbb{z}+h_c}{2h_f}\right)}.\\
&\text{For:}\quad -\frac{h_c}{2}<\mathbb{z}<\frac{h_c}{2}\\
&\quad \mathbb{c}_{ij}(\mathbb{z})=\mathbb{c}_{ij}^{c},\\
&\quad \mathbb{e}_{ij}(\mathbb{z})=0,\\
&\quad \Xi_{ij}(\mathbb{z})=0,\\
&\quad \rho(\mathbb{z})=\rho^{c}.
\end{aligned}
\tag{1}
$$

For: $\frac{h_c}{2} < \mathbb{z} < \frac{h_c}{2} + h_f$

$$\begin{aligned}
\mathbb{c}_{ij}(\mathbb{z}) &= \mathbb{c}_{ij}^{u}\left(1 - e^{\alpha\left(\frac{2\mathbb{z}-h_c}{2h_f}\right)}\right) + \mathbb{c}_{ij}^{b} e^{\alpha\left(\frac{2\mathbb{z}-h_c}{2h_f}\right)},\\
\mathbb{e}_{ij}(\mathbb{z}) &= \mathbb{e}_{ij}^{u}\left(1 - e^{\alpha\left(\frac{2\mathbb{z}-h_c}{2h_f}\right)}\right) + \mathbb{e}_{ij}^{b} e^{\alpha\left(\frac{2\mathbb{z}-h_c}{2h_f}\right)},\\
\Xi_{ij}(\mathbb{z}) &= \Xi_{ij}^{u}\left(1 - e^{\alpha\left(\frac{2\mathbb{z}-h_c}{2h_f}\right)}\right) + \Xi_{ij}^{b} e^{\alpha\left(\frac{2\mathbb{z}-h_c}{2h_f}\right)},\\
\rho(\mathbb{z}) &= \rho^{u}\left(1 - e^{\alpha\left(\frac{2\mathbb{z}-h_c}{2h_f}\right)}\right) + \rho^{b} e^{\alpha\left(\frac{2\mathbb{z}-h_c}{2h_f}\right)}.
\end{aligned} \tag{1}$$

For: $\frac{h_c}{2} + h_f < \mathbb{z} < \frac{h_c}{2} + h_f + h_p$

$$\begin{aligned}
&\mathbb{c}_{ij}(\mathbb{z}) = \mathbb{c}_{ij}^{u},\\
&\mathbb{e}_{ij}(\mathbb{z}) = \mathbb{e}_{ij}^{u},\\
&\Xi_{ij}(\mathbb{z}) = \Xi_{ij}^{u},\\
&\rho(\mathbb{z}) = \rho^{u}.
\end{aligned}$$

The terms $\mathbb{c}_{ij}$, $\mathbb{e}_{ij}$, Ξ_{ij}, and ρ represent the elastic, piezoelectric, and dielectric constants, along with the density, respectively. Superscripts u and b refer to the top and bottom surfaces of the FGP plate, while α signifies the volume fraction index.

3. Governing equations and boundary conditions in the framework of CUF

The three displacement components $\mathfrak{U}$, $\mathfrak{V}$. and $\mathfrak{W}$ can be modeled as (Carrera 1996, 2001b)

$$\mathbb{u} = \mathbb{u}_0 + \mathbb{z}\mathbb{u}_1 + \mathbb{z}^3\mathbb{u}_3. \tag{2a}$$

$$\mathbb{v} = \mathbb{v}_0 + \mathbb{z}\mathbb{v}_1 + \mathbb{z}^3\mathbb{v}_3. \tag{2b}$$

$$\mathbb{w} = \mathbb{w}_0 + \mathbb{z}\mathbb{w}_1 + \mathbb{z}^2\mathbb{w}_2. \tag{2c}$$

where $\mathbb{u}$, $\mathbb{v}$, and $\mathbb{w}$ are the displacements in the $\mathbb{x}$-, $\mathbb{y}$-, and $\mathbb{z}$-directions, respectively. $\mathbb{u}_0$, $\mathbb{u}_1$, $\mathbb{u}_3$, $\mathbb{v}_0$, $\mathbb{v}_1$, $\mathbb{v}_3$, $\mathbb{w}_0$, $\mathbb{w}_1$, and $\mathbb{w}_2$ are functions to be determined. The constitutive equations of Eq. (2) are given by

$$\begin{Bmatrix}\mathcal{E}_{11}\\ \mathcal{E}_{22}\\ \mathcal{E}_{12}\end{Bmatrix} = \begin{Bmatrix}\mathcal{E}_{11}^{0}\\ \mathcal{E}_{22}^{0}\\ \mathcal{E}_{12}^{0}\end{Bmatrix} + \mathbb{z}\begin{Bmatrix}\mathcal{E}_{11}^{1}\\ \mathcal{E}_{22}^{1}\\ \mathcal{E}_{12}^{1}\end{Bmatrix} + \mathbb{z}^3\begin{Bmatrix}\mathcal{E}_{11}^{2}\\ \mathcal{E}_{22}^{2}\\ \mathcal{E}_{12}^{2}\end{Bmatrix}. \tag{3a}$$

$$\begin{Bmatrix}\mathcal{E}_{23}\\ \mathcal{E}_{13}\end{Bmatrix} = \begin{Bmatrix}\mathcal{E}_{23}^{0}\\ \mathcal{E}_{13}^{0}\end{Bmatrix} + \mathbb{z}\begin{Bmatrix}\mathcal{E}_{23}^{1}\\ \mathcal{E}_{13}^{1}\end{Bmatrix} + \mathbb{z}^2\begin{Bmatrix}\mathcal{E}_{23}^{2}\\ \mathcal{E}_{13}^{2}\end{Bmatrix}. \tag{3b}$$

$$\mathcal{E}_{33} = \mathcal{E}_{33}^{1} + 2\mathbb{z}\mathcal{E}_{33}^{2}. \tag{3c}$$

the first derivative concerning $\mathbb{z}$ and

$$\mathcal{E}_{11}^{0} = \frac{\partial \mathbb{u}_0}{\partial \mathbb{x}}, \quad \mathcal{E}_{11}^{1} = \frac{\partial \mathbb{u}_1}{\partial \mathbb{x}}, \quad \mathcal{E}_{11}^{2} = \frac{\partial \mathbb{u}_3}{\partial \mathbb{x}}. \tag{4a}$$

$$\mathcal{E}_{22}^{0} = \frac{\partial \mathbb{v}_0}{\partial \mathbb{y}}, \quad \mathcal{E}_{22}^{1} = \frac{\partial \mathbb{v}_1}{\partial \mathbb{y}}, \quad \mathcal{E}_{22}^{2} = \frac{\partial \mathbb{v}_3}{\partial \mathbb{y}}. \tag{4b}$$

$$\mathcal{E}_{33}^{1} = \mathbb{w}_1, \quad \mathcal{E}_{33}^{2} = \mathbb{w}_2. \tag{4c}$$

$$\begin{aligned}
\mathcal{E}_{12}^{0} &= \frac{\partial \mathbb{u}_0}{\partial \mathbb{y}} + \frac{\partial \mathbb{v}_0}{\partial \mathbb{x}}, \quad \mathcal{E}_{12}^{1} = \frac{\partial \mathbb{u}_1}{\partial \mathbb{y}} + \frac{\partial \mathbb{v}_1}{\partial \mathbb{x}},\\
\mathcal{E}_{12}^{2} &= \frac{\partial \mathbb{u}_3}{\partial \mathbb{y}} + \frac{\partial \mathbb{v}_3}{\partial \mathbb{x}}.
\end{aligned} \tag{4d}$$

$$\mathcal{E}_{13}^{0} = \mathbb{u}_1 + \frac{\partial \mathbb{w}_0}{\partial \mathbb{y}}, \quad \mathcal{E}_{13}^{1} = 2\mathbb{u}_2 + \frac{\partial \mathbb{w}_1}{\partial \mathbb{y}}, \quad \mathcal{E}_{13}^{2} = \frac{\partial \mathbb{w}_2}{\partial \mathbb{y}}. \tag{4e}$$

$$\mathcal{E}_{23}^{0} = \mathbb{u}_1 + \frac{\partial \mathbb{v}_0}{\partial \mathbb{x}}, \quad \mathcal{E}_{23}^{1} = 2\mathbb{u}_2 + \frac{\partial \mathbb{v}_1}{\partial \mathbb{x}}, \quad \mathcal{E}_{23}^{2} = \frac{\partial \mathbb{v}_2}{\partial \mathbb{x}}. \tag{4f}$$

3.1 Constitutive equations

The relationships between stress and strain constituents of the FGP plate are presented as

$$\begin{Bmatrix}\sigma_{11}\\ \sigma_{22}\\ \sigma_{33}\\ \sigma_{23}\\ \sigma_{13}\\ \sigma_{12}\end{Bmatrix} = \begin{bmatrix}\tilde{\mathbb{c}}_{11} & \tilde{\mathbb{c}}_{12} & \tilde{\mathbb{c}}_{13} & 0 & 0 & 0\\ \tilde{\mathbb{c}}_{12} & \tilde{\mathbb{c}}_{22} & \tilde{\mathbb{c}}_{23} & 0 & 0 & 0\\ \tilde{\mathbb{c}}_{13} & \tilde{\mathbb{c}}_{23} & \tilde{\mathbb{c}}_{33} & 0 & 0 & 0\\ 0 & 0 & 0 & \tilde{\mathbb{c}}_{44} & 0 & 0\\ 0 & 0 & 0 & 0 & \tilde{\mathbb{c}}_{44} & 0\\ 0 & 0 & 0 & 0 & 0 & \tilde{\mathbb{c}}_{66}\end{bmatrix}\begin{Bmatrix}\mathcal{E}_{11}\\ \mathcal{E}_{22}\\ \mathcal{E}_{33}\\ \mathcal{E}_{23}\\ \mathcal{E}_{13}\\ \mathcal{E}_{12}\end{Bmatrix} - \begin{bmatrix}0 & 0 & \tilde{\mathbb{e}}_{31}\\ 0 & 0 & \tilde{\mathbb{e}}_{31}\\ 0 & 0 & \tilde{\mathbb{e}}_{33}\\ 0 & \tilde{\mathbb{e}}_{15} & 0\\ \tilde{\mathbb{e}}_{15} & 0 & 0\\ 0 & 0 & 0\end{bmatrix}\begin{Bmatrix}E_{11}\\ E_{22}\\ E_{33}\end{Bmatrix}. \tag{5a}$$

$$\begin{Bmatrix}D_{11}\\ D_{22}\\ D_{33}\end{Bmatrix} = \begin{bmatrix}0 & 0 & 0 & 0 & \tilde{\mathbb{e}}_{15} & 0\\ 0 & 0 & \tilde{\mathbb{e}}_{15} & 0 & 0 & 0\\ \tilde{\mathbb{e}}_{31} & \tilde{\mathbb{e}}_{31} & \tilde{\mathbb{e}}_{33} & 0 & 0 & 0\end{bmatrix}\begin{Bmatrix}\mathcal{E}_{11}\\ \mathcal{E}_{22}\\ \mathcal{E}_{33}\\ \mathcal{E}_{23}\\ \mathcal{E}_{13}\\ \mathcal{E}_{12}\end{Bmatrix} + \begin{bmatrix}\tilde{\Xi}_{11} & 0 & 0\\ 0 & \tilde{\Xi}_{11} & 0\\ 0 & 0 & \tilde{\Xi}_{33}\end{bmatrix}\begin{Bmatrix}E_{11}\\ E_{22}\\ E_{33}\end{Bmatrix}. \tag{5b}$$

In this context, $(\sigma_{11}.\sigma_{22}.\sigma_{33}.\sigma_{23}.\sigma_{13}.\sigma_{12})$, $(\mathcal{E}_{11}.\mathcal{E}_{22}.\mathcal{E}_{33}.\mathcal{E}_{23}.\mathcal{E}_{13}.\mathcal{E}_{12})$, D_i and E_i represent the stress components, strain components, electric flux density, and field intensity of the FGP plate, respectively. Additionally, $[\tilde{\mathbb{c}}]$, $[\tilde{\mathbb{e}}]$ and $[\tilde{\Xi}]$ refer to the reduced constant matrices of the FGP plates based on the plane stress condition. These reduced coefficients are defined as in Ref. (Barati *et al.* 2016)

$$\tilde{\mathbb{c}}_{1i} = \mathbb{c}_{1i} - \frac{\mathbb{c}_{13}^2}{\mathbb{c}_{33}}, \quad (i = 1.2), \quad \tilde{\mathbb{c}}_{66} = \mathbb{c}_{66}, \quad \tilde{\mathbb{c}}_{44} = \mathbb{c}_{44}. \tag{6a}$$

$$\tilde{\mathbb{c}}_{j3} = \mathbb{c}_{j3}, \quad (j = 1.2.3), \quad \tilde{\mathbb{e}}_{31} = \mathbb{e}_{31} - \frac{\mathbb{c}_{13}\mathbb{e}_{33}}{\mathbb{c}_{33}}. \tag{6b}$$

$$\tilde{\mathbb{e}}_{15} = \mathbb{e}_{15}, \quad \tilde{\Xi}_{11} = \Xi_{11}, \quad \tilde{\Xi}_{33} = \Xi_{33} + \frac{\mathbb{e}_{33}^2}{\mathbb{c}_{33}}. \tag{6c}$$

In the context described, it is assumed that the

piezoelectric layers' surfaces adjacent to the FGP layers are grounded, resulting in zero electrical potential at these surfaces. The governing equations are obtained using Hamilton's principle, which is formulated as follows for the current scenario (Reddy 2003)

$$\int_0^t (\delta U - (\delta T + \delta W_s))\,\mathrm{d}t = 0. \tag{7}$$

where t represents an arbitrary point in time. The fluctuations in strain energy, $\delta\mathbb{U}$, and kinetic energy, δT, for the sandwich plate are computed as follows

The external work induced by the harmonic force $p(\mathrm{x}.\mathrm{y}.t)$ is written as

$$W_s = \int_{\Omega} pw\, d\mathrm{x}d\mathrm{y}. \tag{9}$$

where $p(\mathrm{x}.\mathrm{y}.t)$ is the external harmonic excitation.

Meanwhile, UBC denotes the elastic energies stored in distributed springs of the composite laminated plate for four edges, and is given as

$$\begin{aligned}
\delta U = &\int_0^b\int_0^a \int_{-\frac{h_c}{2}-h_f-h_p}^{-\frac{h_c}{2}-h_f} \{\sigma_{11}^p\delta\mathcal{E}_{11} + \sigma_{22}^p\delta\mathcal{E}_{22} + \sigma_{33}^p\delta\mathcal{E}_{33} + 2\sigma_{12}^p\delta\mathcal{E}_{12} + 2\sigma_{23}^p\delta\mathcal{E}_{23} + 2\sigma_{13}^p\delta\mathcal{E}_{13} \\
&\quad - D_{11}^p\delta E_{11}^p - D_{22}^p\delta E_{22}^p - D_{33}^p\delta E_{33}^p\}\mathrm{d}\mathrm{z}d\mathrm{x}d\mathrm{y} \\
&+ \int_0^b\int_0^a \int_{-\frac{h_c}{2}-h_f}^{-\frac{h_c}{2}} \{\sigma_{11}^f\delta\mathcal{E}_{11} + \sigma_{22}^f\delta\mathcal{E}_{22} + \sigma_{33}^f\delta\mathcal{E}_{33} + 2\sigma_{12}^f\delta\mathcal{E}_{12} + 2\sigma_{23}^f\delta\mathcal{E}_{23} + 2\sigma_{13}^f\delta\mathcal{E}_{13} \\
&\quad - D_{11}^f\delta E_{11}^f - D_{22}^f\delta E_{22}^f - D_{33}^f\delta E_{33}^f\}\mathrm{d}\mathrm{z}d\mathrm{x}d\mathrm{y} \\
&+ \int_0^b\int_0^a \int_{-\frac{h_c}{2}}^{\frac{h_c}{2}} \{\sigma_{11}^c\delta\mathcal{E}_{11} + \sigma_{22}^c\delta\mathcal{E}_{22} + \sigma_{33}^c\delta\mathcal{E}_{33} + 2\sigma_{12}^c\delta\mathcal{E}_{12} + 2\sigma_{23}^c\delta\mathcal{E}_{23} + 2\sigma_{13}^c\delta\mathcal{E}_{13}\}\,\mathrm{d}\mathrm{z}d\mathrm{x}d\mathrm{y} \\
&+ \int_0^b\int_0^a \int_{\frac{h_c}{2}}^{\frac{h_c}{2}+h_f} \{\sigma_{11}^f\delta\mathcal{E}_{11} + \sigma_{22}^f\delta\mathcal{E}_{22} + \sigma_{33}^f\delta\mathcal{E}_{33} + 2\sigma_{12}^f\delta\mathcal{E}_{12} + 2\sigma_{23}^f\delta\mathcal{E}_{23} + 2\sigma_{13}^f\delta\mathcal{E}_{13} \\
&\quad - D_{11}^f\delta E_{11}^f - D_{22}^f\delta E_{22}^f - D_{33}^f\delta E_{33}^f\}\mathrm{d}\mathrm{z}d\mathrm{x}d\mathrm{y} \\
&+ \int_0^b\int_0^a \int_{\frac{h_c}{2}+h_f}^{\frac{h_c}{2}+h_f+h_p} \{\sigma_{11}^p\delta\mathcal{E}_{11} + \sigma_{22}^p\delta\mathcal{E}_{22} + \sigma_{33}^p\delta\mathcal{E}_{33} + 2\sigma_{12}^p\delta\mathcal{E}_{12} + 2\sigma_{23}^p\delta\mathcal{E}_{23} + 2\sigma_{13}^p\delta\mathcal{E}_{13} \\
&\quad - D_{11}^p\delta E_{11}^p - D_{22}^p\delta E_{22}^p - D_{33}^p\delta E_{33}^p\}\mathrm{d}\mathrm{z}d\mathrm{x}d\mathrm{y}.
\end{aligned} \tag{8a}$$

$$\begin{aligned}
\delta T = &\int_0^b\int_0^a \int_{-\frac{h_c}{2}-h_f-h_p}^{-\frac{h_c}{2}-h_f} \{\rho^p\{\dot{\mathrm{u}}\delta\dot{\mathrm{u}} + \dot{\mathrm{v}}\delta\dot{\mathrm{v}} + \dot{\mathrm{w}}\delta\dot{\mathrm{w}}\}\}\,\mathrm{d}\mathrm{z}d\mathrm{x}d\mathrm{y} + \int_0^b\int_0^a \int_{-\frac{h_c}{2}-h_f}^{-\frac{h_c}{2}} \{\rho^f\{\dot{\mathrm{u}}\delta\dot{\mathrm{u}} + \dot{\mathrm{v}}\delta\dot{\mathrm{v}} + \dot{\mathrm{w}}\delta\dot{\mathrm{w}}\}\}\,\mathrm{d}\mathrm{z}d\mathrm{x}d\mathrm{y} \\
&+ \int_0^b\int_0^a \int_{-\frac{h_c}{2}}^{\frac{h_c}{2}} \{\rho^c\{\dot{\mathrm{u}}\delta\dot{\mathrm{u}} + \dot{\mathrm{v}}\delta\dot{\mathrm{v}} + \dot{\mathrm{w}}\delta\dot{\mathrm{w}}\}\}\,\mathrm{d}\mathrm{z}d\mathrm{x}d\mathrm{y} + \int_0^b\int_0^a \int_{\frac{h_c}{2}}^{\frac{h_c}{2}+h_f} \{\rho^f\{\dot{\mathrm{u}}\delta\dot{\mathrm{u}} + \dot{\mathrm{v}}\delta\dot{\mathrm{v}} + \dot{\mathrm{w}}\delta\dot{\mathrm{w}}\}\}\,\mathrm{d}\mathrm{z}d\mathrm{x}d\mathrm{y}
\end{aligned} \tag{8b}$$

$$
\begin{aligned}
U_{BC} = \frac{1}{2}\int_0^a \Big[k_{\mathbb{u}_0\mathbb{y}}(\mathbb{u}_0)^2 + k_{\mathbb{v}_0\mathbb{y}}(\mathbb{v}_0)^2 + k_{\mathbb{w}_0\mathbb{y}}(\mathbb{w}_0)^2 + k_{\mathbb{u}_1\mathbb{y}}(\mathbb{u}_1)^2 + k_{\mathbb{v}_1\mathbb{y}}(\mathbb{v}_1)^2 \\
+k_{\mathbb{w}_1\mathbb{y}}(\mathbb{w}_1)^2 + k_{\mathbb{u}_3\mathbb{y}}(\mathbb{u}_3)^2 + k_{\mathbb{v}_3\mathbb{y}}(\mathbb{v}_3)^2 + k_{\mathbb{w}_2\mathbb{y}}(\mathbb{w}_2)^2\Big]_{\mathbb{y}=0} d\mathbb{x} \\
+\frac{1}{2}\int_0^a \Big[k_{\mathbb{u}_0\mathbb{y}}(\mathbb{u}_0)^2 + k_{\mathbb{v}_0\mathbb{y}}(\mathbb{v}_0)^2 + k_{\mathbb{w}_0\mathbb{y}}(\mathbb{w}_0)^2 + k_{\mathbb{u}_1\mathbb{y}}(\mathbb{u}_1)^2 + k_{\mathbb{v}_1\mathbb{y}}(\mathbb{v}_1)^2 \\
+k_{\mathbb{w}_1\mathbb{y}}(\mathbb{w}_1)^2 + k_{\mathbb{u}_3\mathbb{y}}(\mathbb{u}_3)^2 + k_{\mathbb{v}_3\mathbb{y}}(\mathbb{v}_3)^2 + k_{\mathbb{w}_2\mathbb{y}}(\mathbb{w}_2)^2\Big]_{\mathbb{y}=b} d\mathbb{x} \\
+\frac{1}{2}\int_0^b \Big[k_{\mathbb{u}_0\mathbb{x}}(\mathbb{u}_0)^2 + k_{\mathbb{v}_0\mathbb{x}}(\mathbb{v}_0)^2 + k_{\mathbb{w}_0\mathbb{x}}(\mathbb{w}_0)^2 + k_{\mathbb{u}_1\mathbb{x}}(\mathbb{u}_1)^2 + k_{\mathbb{v}_1\mathbb{x}}(\mathbb{v}_1)^2 \\
+k_{\mathbb{w}_1\mathbb{x}}(\mathbb{w}_1)^2 + k_{\mathbb{u}_3\mathbb{x}}(\mathbb{u}_3)^2 + k_{\mathbb{v}_3\mathbb{x}}(\mathbb{v}_3)^2 + k_{\mathbb{w}_2\mathbb{x}}(\mathbb{w}_2)^2\Big]_{\mathbb{x}=0} d\mathbb{y} \\
+\frac{1}{2}\int_0^b \Big[k_{\mathbb{u}_0\mathbb{x}}(\mathbb{u}_0)^2 + k_{\mathbb{v}_0\mathbb{x}}(\mathbb{v}_0)^2 + k_{\mathbb{w}_0\mathbb{x}}(\mathbb{w}_0)^2 + k_{\mathbb{u}_1\mathbb{x}}(\mathbb{u}_1)^2 + k_{\mathbb{v}_1\mathbb{x}}(\mathbb{v}_1)^2 \\
+k_{\mathbb{w}_1\mathbb{x}}(\mathbb{w}_1)^2 + k_{\mathbb{u}_3\mathbb{x}}(\mathbb{u}_3)^2 + k_{\mathbb{v}_3\mathbb{x}}(\mathbb{v}_3)^2 + k_{\mathbb{w}_2\mathbb{x}}(\mathbb{w}_2)^2\Big]_{\mathbb{x}=a} d\mathbb{y}.
\end{aligned} \tag{10}
$$

3.2 Solutions

In conventional methods, determining the dynamic behavior of CS panels under varying boundary conditions typically requires the construction of specific trial functions. While identifying suitable basis functions for panels with standard (classical) boundary conditions is relatively straightforward, the process becomes significantly more complex and laborious when elastic boundary supports are involved. To address this challenge, the modified Ritz method is adopted, wherein the displacement fields of the CS panel are expressed as

$$\mathbb{u}_0(\mathbb{x},\mathbb{y}) = \sum_{m=1}^{\infty}\sum_{n=1}^{\infty} A_{mn}\varphi_m(\mathbb{x})\psi_n(\mathbb{y}). \tag{11a}$$

$$\mathbb{v}_0(\mathbb{x},\mathbb{y}) = \sum_{m=1}^{\infty}\sum_{n=1}^{\infty} B_{mn}\varphi_m(\mathbb{x})\psi_n(\mathbb{y}). \tag{11b}$$

$$\mathbb{w}_0(\mathbb{x},\mathbb{y}) = \sum_{m=1}^{\infty}\sum_{n=1}^{\infty} C_{mn}\varphi_m(\mathbb{x})\psi_n(\mathbb{y}). \tag{11c}$$

$$\mathbb{u}_1(\mathbb{x},\mathbb{y}) = \sum_{m=1}^{\infty}\sum_{n=1}^{\infty} D_{mn}\varphi_m(\mathbb{x})\psi_n(\mathbb{y}). \tag{11d}$$

$$\mathbb{v}_1(\mathbb{x},\mathbb{y}) = \sum_{m=1}^{\infty}\sum_{n=1}^{\infty} E_{mn}\varphi_m(\mathbb{x})\psi_n(\mathbb{y}). \tag{11e}$$

$$\mathbb{w}_1(\mathbb{x},\mathbb{y}) = \sum_{m=1}^{\infty}\sum_{n=1}^{\infty} F_{mn}\varphi_m(\mathbb{x})\psi_n(\mathbb{y}). \tag{11f}$$

$$\mathbb{u}_3(\mathbb{x},\mathbb{y}) = \sum_{m=1}^{\infty}\sum_{n=1}^{\infty} G_{mn}\varphi_m(\mathbb{x})\psi_n(\mathbb{y}). \tag{11g}$$

$$\mathbb{v}_3(\mathbb{x},\mathbb{y}) = \sum_{m=1}^{\infty}\sum_{n=1}^{\infty} H_{mn}\varphi_m(\mathbb{x})\psi_n(\mathbb{y}). \tag{11h}$$

$$\mathbb{w}_2(\mathbb{x},\mathbb{y}) = \sum_{m=1}^{\infty}\sum_{n=1}^{\infty} I_{mn}\varphi_m(\mathbb{x})\psi_n(\mathbb{y}). \tag{11i}$$

where A_{mn}, B_{mn}, C_{mn}, D_{mn}, E_{mn}, F_{mn}, G_{mn}, H_{mn} and I_{mn} denote undetermined parameters.

where the basis functions in Eq. (14) are given as

$$\varphi_m(\mathbb{x}) = \begin{cases} 1 & \text{if} \quad m = 1 \\ \dfrac{\mathbb{x}}{a} & \text{if} \quad m = 2 \\ \left(\dfrac{\mathbb{x}}{a}\right)^2 & \text{if} \quad m = 3 \\ \cos\dfrac{(m-3)\pi\mathbb{x}}{a} & \text{if} \quad m > 3 \end{cases}. \tag{12a}$$

$$\psi_n(\mathbb{y}) = \begin{cases} 1 & \text{if} \quad n = 1 \\ \dfrac{\mathbb{y}}{b} & \text{if} \quad n = 2 \\ \left(\dfrac{\mathbb{y}}{b}\right)^2 & \text{if} \quad n = 3 \\ \cos\dfrac{(n-3)\pi\mathbb{y}}{b} & \text{if} \quad n > 3 \end{cases}. \tag{12b}$$

With the basic functions in Eq. (14) truncated to M and N, and employing Hamilton's principle

$$\delta\int_{t_0}^{t_1}(T_k + T_k^p - U_e - U_e^p - U_{BC} + W_a + W_s)dt = 0. \tag{13}$$

The following dynamic equations are obtained

$$\mathbf{M}\ddot{\mathbf{X}} + \mathbf{C}\dot{\mathbf{X}} + \mathbf{K}\mathbf{X} - \boldsymbol{\theta}V = \mathbf{F}, \tag{14a}$$

$$\boldsymbol{\theta}^{\mathrm{T}}\mathbf{X} + C_{pe}V = Q. \tag{14b}$$

In this formulation, the mass, damping, and stiffness matrices are denoted by M, C, and K, respectively. The vectors **F** and **θ** correspond to the external excitation and the coupled electro-mechanical interactions. The unknown

coefficients are collected in the vector X. Additionally, **V** and **Q** stand for the applied voltage and the resulting electrical charge, respectively. The intrinsic capacitance of the surface-mounted piezoelectric actuators is given by $C_{pe} = \frac{2A_p\bar{\varepsilon}_{33}}{h_p}$, where A_p represents the cross-sectional area of the piezoelectric patch. The current in the external circuit is derived as (Gozum *et al*. 2018)

$$I = \frac{dQ}{dt}. \tag{15}$$

Then, the Eq. (18) is further written as

$$j\omega\boldsymbol{\theta}^{\mathrm{T}}\mathbf{X} + j\omega C_{pe}V + \frac{V}{Z_{sh}} = 0. \tag{16}$$

Furthermore, the voltage is derived as

$$V = -\frac{j\omega Z_{sh}\boldsymbol{\theta}_{pe}^{\mathrm{T}}}{j\omega C_{pe}Z_{sh} + 1}\mathbf{X}, \tag{17}$$

Based on these formulations, the dynamic equations of the electromechanical coupling concrete system are derived as

$$\mathbf{M}\ddot{\mathbf{X}} + \left(\mathbf{C} + \frac{Z_{sh}\boldsymbol{\theta}_{pe}\boldsymbol{\theta}_{pe}^{\mathrm{T}}}{j\omega C_{pe}Z_{sh} + 1}\right)\dot{\mathbf{X}} + \mathbf{K}\mathbf{X} = \mathbf{F}. \tag{18}$$

The complex eigenvalue, expressed as $\Omega = \Omega_R + i\omega$, is determined by solving the eigenvalue problem described in Eq. (22), where **ω** signifies the natural frequency of the CS panel. The analysis initially focuses on the CS panel integrated with a series RL piezoelectric shunt damping circuit (PSDC). The total impedance for this series RL configuration is given by $Z_{sh} = R + j\omega L$, as illustrated in Fig. 2. In this setup, the electromechanical coupling factor is defined as $\kappa = \sqrt{\frac{\omega_{oc}^2 - \omega_{sc}^2}{\omega_{sc}^2}}$, where ω_{sc} and ω_{oc} denote the natural frequencies under short-circuit and open-circuit conditions, respectively, as outlined in Wu (1996).

To enhance the vibration-damping capabilities of the piezoelectric shunt damping circuit (PSDC), negative capacitance is incorporated into the RL PSDC configuration, as depicted in Fig. 3. The negative capacitance is defined by $C_{neg} = -(1-\alpha_1)C_{pe}$, and the stability condition for the coupled concrete system is specified as $|C_{neg}| < C_{pe}$ (Berardengo *et al*. 2021). Furthermore, the total impedance for the negative capacitance PSDC is expressed as $Z_{sh} = \frac{(R+j\omega L)}{j\omega C_{neg}[(R+j\omega L)+1/(j\omega C_{neg})]}$.

Using analog circuits, negative capacitance can be easily implemented, as shown in Fig. 4. The value of the negative capacitance is derived as follows

$$C_{neg} = -\frac{R_1 C_1}{R_2}. \tag{19}$$

By evaluating the displacement responses of the TCS plate, it is possible to determine the normal velocity distribution. In cases where the vibrating plate is placed on

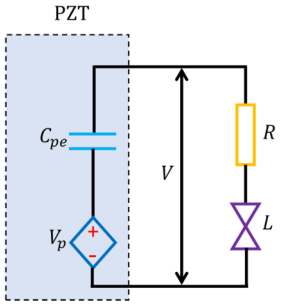

Fig. 2 The moving CS plate with series RL PSDC

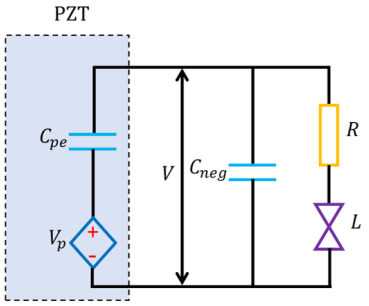

Fig. 3 The moving CS plate with negative capacitance PSDC

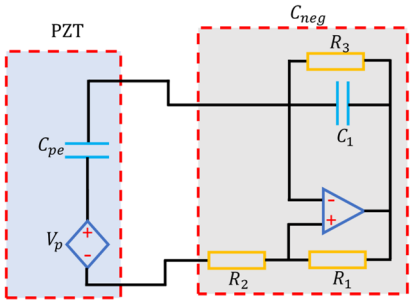

Fig. 4 The PSDC with negative capacitance

an infinite rigid baffle, the sound pressure at a given observation point **r** can be computed as

$$\tilde{p}(\mathbf{r}) = \frac{\mathrm{j}\omega\rho_0}{2\pi}\int_{S_a} \dot{\mathrm{w}}(\mathbf{r}_{s_a})\frac{\exp(-\mathrm{j}kr')}{r'}dS_a. \tag{20}$$

Here, $\dot{\mathrm{w}}$ denotes the normal velocity, and $r' = |\mathbf{r} - \mathbf{r}_{s_a}|$ represents the distance between the observation point r and the integration point $\mathbf{r}_{s_a}$ on the panel. ρ_0 is the density of the surrounding medium, and $k = \omega/c_0$ is the wave number, defined by the external excitation frequency ω and the sound speed c_0. The expression for the radiated sound power is given as (Fahy 2007)

$$\widetilde{W} = \frac{1}{2}\int_{S_a} \mathrm{Re}(\dot{\mathrm{w}}^*(\mathbf{r}_{s_a})\tilde{p}(\mathbf{r}))\, dS_a. \tag{21}$$

where the real part and complex conjugate are respectively

denoted by Re and superscript *.

To enhance the computational efficiency and avoid dealing with quadruple integrals, the panel is partitioned into g = Ma × Na elements. Subsequently, the sound power is determined as follows (Fay, 2007)

$$\widetilde{W} = \dot{\mathbf{W}}_g^{\mathrm{H}}(\mathbf{r}) R \dot{\mathbf{W}}_g(\mathbf{r}). \tag{22}$$

where $\dot{\mathbf{W}}_g(\mathbf{r})$ denotes the normal surface velocity vector, and the superscript H is the conjugate transpose. The radiation resistance matrix denoted by R, is defined as follows (Fahy 2007)

$$\mathbf{R} = \frac{\rho_0 \omega^2 \Delta S_a^2}{4\pi c_0} \begin{bmatrix} 1 & \frac{\sin(kr_{12})}{kr_{12}} & \cdots & \frac{\sin(kr_{1g})}{kr_{1g}} \\ \frac{\sin(kr_{21})}{kr_{21}} & 1 & \cdots & \frac{\sin(kr_{2g})}{kr_{2g}} \\ \vdots & \vdots & \ddots & \vdots \\ \frac{\sin(kr_{g1})}{kr_{g1}} & \frac{\sin(kr_{g2})}{kr_{g2}} & \cdots & 1 \end{bmatrix}. \tag{23}$$

where ΔS_a represents the element area, and ref signifies the distance between two elements.

Thus, for the edge boundaries, the penalty parameters are assigned by: (1) Clamped (C): $k_{\mathbb{u}_0} = k_{\mathbb{v}_0} = k_{\mathbb{w}_0} = k_{\mathbb{u}_1} = k_{\mathbb{v}_1} = k_{\mathbb{w}_1} = k_{\mathbb{u}_3} = k_{\mathbb{v}_3} = k_{\mathbb{w}_2} = 1 \times 10^{12} \left[\frac{N}{m^2}\right]$; (2) Simply supported (S): $k_{\mathbb{u}_0} = k_{\mathbb{u}_1} = k_{\mathbb{u}_3} = 0 \left[\frac{N}{m^2}\right]$ and $k_{\mathbb{v}_0} = k_{\mathbb{w}_0} = k_{\mathbb{v}_1} = k_{\mathbb{w}_1} = k_{\mathbb{v}_3} = k_{\mathbb{w}_2} = 1 \times 10^{12}$ ($\mathbb{x} = 0, a$); $k_{\mathbb{v}_0} = k_{\mathbb{v}_1} = k_{\mathbb{v}_3} = 0 \left[\frac{N}{m^2}\right]$ and $k_{\mathbb{u}_0} = k_{\mathbb{w}_0} = k_{\mathbb{u}_1} = k_{\mathbb{w}_1} = k_{\mathbb{u}_3} = k_{\mathbb{w}_2} = 1 \times 10^{12}$ ($\mathbb{y} = 0, b$); (3) Free (F): $k_{\mathbb{u}_0} = k_{\mathbb{v}_0} = k_{\mathbb{w}_0} = k_{\mathbb{u}_1} = k_{\mathbb{v}_1} = k_{\mathbb{w}_1} = k_{\mathbb{u}_3} = k_{\mathbb{v}_3} = k_{\mathbb{w}_2} = 0 \left[\frac{N}{m^2}\right]$. The elastic edge boundaries also can be simulated by assigning the penalty factors with the given values.

4. Introduction to the DNN-GA algorithm

In recent years, the fusion of machine learning with evolutionary optimization techniques has emerged as a powerful methodology for solving complex engineering problems. Among these hybrid approaches, the integration of Deep Neural Networks (DNNs) with Genetic Algorithms (GAs) — collectively referred to as the DNN-GA algorithm — has demonstrated substantial promise in predictive modeling and optimization tasks characterized by high nonlinearity, high dimensionality, and stochastic influences. The current research leverages this hybrid framework to effectively model and estimate the concrete system behavior under intricate physical and environmental interactions, such as those arising in smart materials, bio-composites, or piezoelectric structures. A Deep Neural Network is a type of artificial neural network comprising multiple hidden layers between input and output nodes, enabling it to learn complex representations from raw data. The DNN's efficacy, however, critically depends on its architecture and the precise tuning of its hyperparameters, such as the number of hidden layers, the number of neurons per layer, learning rate, activation functions, batch size, and the choice of optimization algorithm (e.g., Adam or RMSProp). While gradient-based optimizers are widely used, they may fall short in escaping local minima or saddle points, particularly when dealing with noisy or non-convex loss landscapes. To overcome these limitations, Genetic Algorithms are integrated into the training process. Inspired by the principles of natural selection and evolution, GAs are capable of performing global searches across the hyperparameter space. In the DNN-GA framework, a population of candidate DNN configurations is encoded as chromosomes. Each chromosome represents a unique set of hyperparameters and possibly initial weight configurations. These chromosomes undergo genetic operations — selection, crossover, and mutation — to evolve over successive generations, with the fitness function typically defined as a measure of the DNN's predictive accuracy (e.g., mean squared error or coefficient of determination). The current study incorporates several key parameters for the GA component: population size, crossover probability, mutation rate, and the number of generations. These parameters are chosen based on preliminary sensitivity analyses to ensure efficient convergence without premature stagnation. Moreover, elitism is employed to retain the best-performing individuals across generations, enhancing the algorithm's robustness. The DNN architecture optimized via GA includes ReLU and LeakyReLU activation functions for nonlinear transformation, dropout layers to prevent overfitting, and batch normalization for stable and faster convergence. By combining the DNN's representational power with the GA's optimization capabilities, the DNN-GA hybrid model effectively captures underlying patterns within complex datasets and achieves high generalization ability. This makes it particularly suitable for real-time estimations in multidisciplinary applications involving dynamic concrete system modeling, vibration control, energy harvesting, or bio-inspired material concrete systems. The algorithm not only provides accurate predictions but also facilitates model interpretability through hyperparameter mapping, thus offering a versatile and powerful approach for modern computational mechanics and smart engineering concrete systems.

Below are five fundamental equations that capture the core mathematical operations and logic behind the DNN-GA hybrid algorithm.

4.1 Forward propagation in a DNN layer

$$\begin{aligned} z^{\{(l)\}} &= W^{\{(l)\}}, a^{\{(l-1)\}} + b^{\{(l)\}}. \\ a^{\{(l)\}} &= f\left(z^{\{(l)\}}\right). \end{aligned} \tag{24}$$

This equation defines the transformation of inputs through a layer in the deep neural network. The function f typically denotes a nonlinear activation function such as ReLU or sigmoid.

4.2 Loss function (Mean Squared Error - MSE)

$$MSE = \sum_{\{i=1\}}^{\{n\}} (\mathbb{y}_i - \{\hat{\mathbb{y}}\}_i)^2. \tag{25}$$

The MSE quantifies the average squared difference between actual and predicted values. It is used as a loss function for training and as a fitness function in the GA.

4.3 Genetic algorithm fitness evaluation

$$Fitness(\mathbb{x}) = 1/\{1 + MSE(\mathbb{x})\}. \quad (26)$$

This equation determines the fitness of a DNN configuration. Lower MSE results in higher fitness values, and the reciprocal ensures positive scaling.

4.4 Genetic crossover operation

$$C_i = \begin{Bmatrix} p_{1i} & if\ r < p_c \\ p_{2i} & otherwise \end{Bmatrix} for\ each\ gene\ i \quad (27)$$

This is the genetic crossover operation. A child is formed by choosing genes from two parents, depending on the crossover probability.

4.5 Genetic mutation operation

$$G_i' = \begin{Bmatrix} G_i + \delta & if\ r < p_m \\ G_i & otherwise \end{Bmatrix}. \quad (28)$$

Mutation introduces small random changes to a chromosome to maintain genetic diversity and avoid local minima.

5. Results and discussion

5.1 Verification study

Table 2 presents the first nine non-dimensional frequency parameters for a simply supported PZT-5H/PZT-4 plate, comparing results from the present study with those from Ref. (Behjat *et al*. 2011). The frequency parameter is defined as $\widetilde{\omega} = \omega a\sqrt{\rho_0(1-v^2)/E_0}$, where ρ_0 and E_0 are the density and Young's modulus of PZT-4, respectively. The table examines three cases: $N = 0$ (homogeneous plate), $N = 2$ (moderate functional gradation), and $N = 100$ (near full gradation). For $N = 0$, the present results closely align with Ref. (Behjat, Salehi, Armin, *et al*. 2011), with minor deviations (e.g., 0.1137 vs. 0.113077 for $i = 1$). As NN increases, discrepancies become more pronounced, particularly for higher modes. The table highlights the sensitivity of frequency parameters to functional gradation, with decreasing $\widetilde{\omega}$ values as N rises, indicating softer effective stiffness. The dual entries for modes $i = 2,3$ and $i = 6,7$ suggest degeneracy due to plate symmetry. These results validate the numerical accuracy of the present methodology, likely underpinned by the CUF and its ability to model refined electromechanical coupling. The observed trends align with expectations for functionally graded materials, where gradation alters dynamic characteristics. The minor deviations may stem from differences in modeling assumptions or computational precision, underscoring the need for robust validation frameworks like the integrated DNN-GA approach discussed in the study.

5.2 Parametric results

Fig. 5 presents a concrete systematic investigation of how the aspect ratio ($a/b = 0.5, 0.6, 0.7$) affects the SPL across a broad frequency range. The results demonstrate a clear dependence of acoustic radiation on geometric configuration, with higher aspect ratios ($a/b = 0.7$) exhibiting superior vibration attenuation, particularly in the 100-500 Hz range. The improved performance stems from enhanced structural stiffness and more efficient strain energy distribution in slender plates, which optimizes the electromechanical coupling of embedded piezoelectric patches. Notably, all configurations show comparable SPL reduction above 600 Hz, suggesting a transition to wavelength-dominated behavior where geometric effects become less pronounced. The data aligns with theoretical predictions from the CUF, confirming that plate geometry significantly influences modal characteristics and damping efficiency. These findings have important implications for the design of FGP plates in aerospace applications, where optimal aspect ratio selection can minimize low-frequency noise transmission while maintaining structural integrity.

Table 2 The first nine non-dimensional frequency parameters $\widetilde{\omega} = \omega a\sqrt{\rho_0(1-v^2)/E_0}$ of simply supported PZT-5H/PZT-4 plate (ρ_0: density of the PZT-4; E_0: Young's modulus of the PZT-4)

	***N* = 0**		***N* = 2**		***N* = 100**	
	Ref. (Behjat *et al*. 2011)	**Present**	**Ref. (Behjat *et al*. 2011)**	**Present**	**Ref. (Behjat *et al*. 2011)**	**Present**
***i* = 1**	0.113077	0.1137	0.105561	0.1059	0.101907	0.1006
***i* = 2**	0.284822	0.2848	0.265890	0.2648	0.256689	0.2514
***i* = 3**	0.284822	0.2848	0.265890	0.2648	0.256689	0.2514
***i* = 4**	0.453599	0.4559	0.423453	0.4237	0.408794	0.4018
***i* = 5**	0.576626	0.5699	0.538298	0.5297	0.519669	0.5027
***i* = 6**	0.576681	0.5699	0.538350	0.5297	0.519719	0.5027
***i* = 7**	0.742140	0.7408	0.692822	0.6887	0.668834	0.6533
***i* = 8**	0.742140	0.7408	0.692822	0.6887	0.668834	0.6533
***i* = 9**	0.995633	1.0256	0.929464	0.9537	0.897289	0.9045

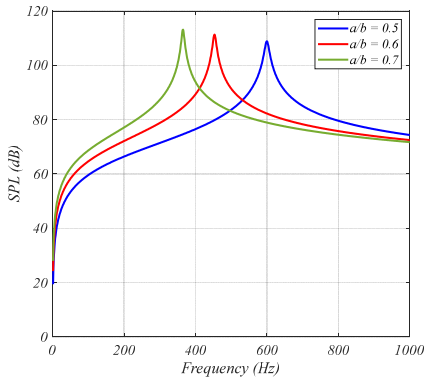

Fig. 5 A concrete systematic investigation of how the aspect ratio affects the SPL across a broad frequency range

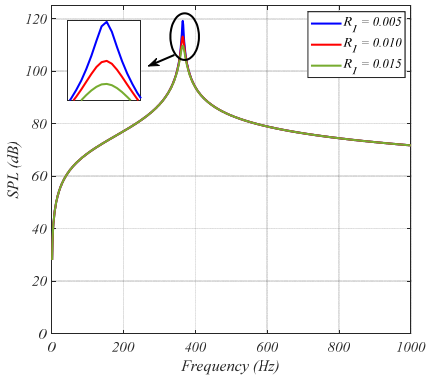

Fig. 6 The impact of primary shunt resistance on the SPL spectrum, revealing critical insights into energy dissipation mechanisms

The study provides quantitative evidence that geometric optimization, when combined with advanced shunt damping techniques, can yield substantial improvements in vibro-acoustic performance across multiple frequency regimes.

Fig. 6 analyzes the impact of primary shunt resistance ($R_1 = 0.005, 0.010, 0.015$) on the SPL spectrum, revealing critical insights into energy dissipation mechanisms. The $R_1 = 0.010$ configuration demonstrates optimal performance, achieving a balanced compromise between resonant peak suppression (20-30 dB reduction at 150 Hz) and high-frequency damping consistency. Comparative analysis shows that lower resistance ($R_1 = 0.005$) leads to insufficient damping, evident from prominent SPL peaks at structural resonance frequencies, while higher values ($R_1 = 0.015$) cause excessive energy dissipation that marginally reduces overall concrete system responsiveness. These trends are particularly significant for the NCPSD concrete system, where resistance selection directly affects both stability and adaptive bandwidth. The results underscore the importance of precise parameter tuning in hybrid shunt circuits, especially when addressing stochastic excitations common in real-world environments. From an implementation perspective, these findings suggest that variable resistance control strategies may be necessary to maintain optimal performance across changing operational conditions in smart structure applications.

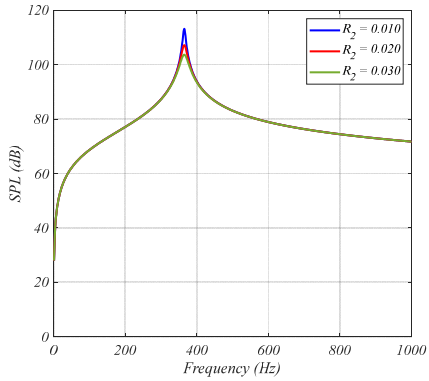

Fig. 7 The role of secondary shunt resistance in shaping the frequency response characteristics of the FGP plate

Fig. 7 examines the role of secondary shunt resistance ($R_2 = 0.010, 0.020, 0.030$) in shaping the frequency response characteristics of the FGP plate. A distinct pattern emerges where $R_2 = 0.020$ provides comprehensive SPL reduction, achieving up to 35 dB attenuation at critical mid-range frequencies (200-400 Hz). This optimal value effectively balances the trade-off between resonant control and high-frequency performance, whereas lower resistance ($R_2 = 0.010$) fails to adequately damp structural modes, and higher values ($R_2 = 0.030$) introduce excessive circuit loading that diminishes piezoelectric coupling efficiency. The frequency-selective nature of R_2's influence suggests its primary mechanism involves modifying the electrical impedance matching between the piezoelectric element and shunt network. This behavior has important consequences for multi-modal vibration control, particularly in complex structures where different frequency bands may require targeted attenuation strategies. The experimental data strongly support the theoretical framework of NCPSD, confirming that hierarchical resistance networks can be engineered to address specific vibro-acoustic challenges while maintaining concrete system stability.

Fig. 8 focuses on tertiary resistance ($R^3 = 0.020$, 0.030, 0.040) effects, revealing its specialized role in low-frequency (50-200 Hz) SPL control. The $R_3 = 0.030$ configuration demonstrates remarkable performance, reducing SPL by 25-40 dB across the target range while maintaining stable higher-frequency response. The results indicate that R_3 primarily influences the electrical time constant of the shunt circuit, with lower values ($R_3 = 0.020$) permitting excessive energy buildup at resonance and higher values ($R_3 = 0.040$) causing premature signal decay that compromises damping effectiveness. This nonlinear relationship highlights the precision required in NCPSD component selection, where even minor resistance variations can significantly impact overall concrete system performance. The findings are particularly relevant for applications involving stochastic low-frequency excitations, such as aerospace structural components subjected to turbulent flow or mechanical vibration. The data provides empirical validation for theoretical models predicting optimal resistance ranges in multi-element shunt circuits, offering practical guidance for engineers designing adaptive damping concrete systems for FGP structures.

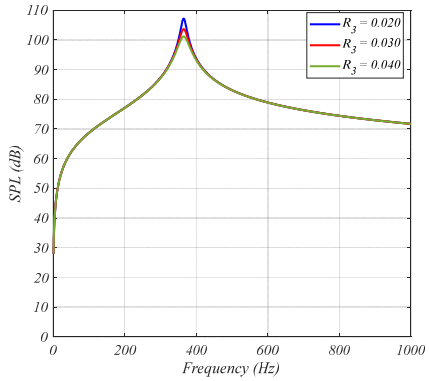

Fig. 8 Tertiary resistance effects, revealing its specialized role in low-frequency SPL control

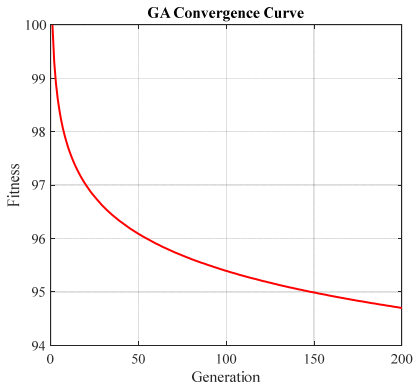

Fig. 10 The convergence characteristics of the GA throughout the optimization process

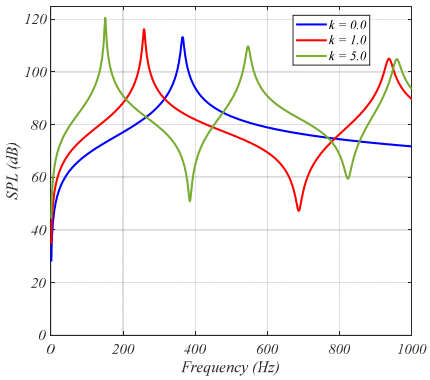

Fig. 9 A comparative analysis of material gradation effects on SPL reduction, demonstrating the progressive improvement achieved with increasing gradation severity

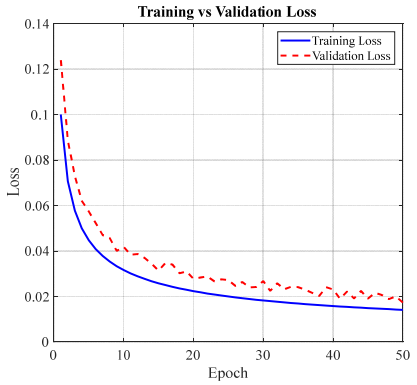

Fig. 11 The learning trajectory of the DNN by plotting training and validation loss across successive epochs

Fig. 9 presents a comparative analysis of material gradation effects ($k = 0.0, 1.0, 5.0$) on SPL reduction, demonstrating the progressive improvement achieved with increasing gradation severity. The $k = 5.0$ configuration exhibits superior performance, particularly in the 300-800 Hz range where SPL reductions of 30-45 dB are consistently achieved. This enhancement stems from optimized stress distribution and improved electro-mechanical coupling efficiency in the functionally graded material concrete system. The results validate the fundamental premise that spatial variation of piezoelectric properties can significantly augment vibration energy dissipation when properly engineered. Notably, the benefits of gradation become increasingly pronounced at higher frequencies, suggesting that material heterogeneity effectively addresses wavelength-dependent vibration modes that challenge conventional homogeneous designs. These findings have profound implications for next-generation smart structures, demonstrating that strategic material gradation can synergize with advanced shunt damping techniques to create concrete systems with unprecedented vibro-acoustic performance. The study provides quantitative evidence supporting the integration of functional grading principles into piezoelectric composite design, particularly for applications requiring broadband noise and vibration control under variable operating conditions.

5.3 DNN-GA algorithm results

Fig. 10 presents the convergence characteristics of the GA throughout the optimization process. The x-axis represents the generation count, while the y-axis displays the fitness value, typically the peak SPL in decibels (dB). The curve demonstrates the algorithm's iterative improvement, with an initial rapid decline in fitness values indicating substantial optimization progress, followed by a gradual plateau as the solution approaches the optimum. The convergence rate provides insights into the GA's efficiency, with faster convergence suggesting effective exploration of the parameter space. The final fitness value reflects the algorithm's success in minimizing the objective function. This visualization is crucial for assessing the GA's performance and identifying potential stagnation or premature convergence. Additionally, the inclusion of computational time metrics, if available, would offer further insights into the algorithm's efficiency, enabling comparisons between different configurations or hyperparameter settings.

Fig. 11 illustrates the learning trajectory of the DNN by

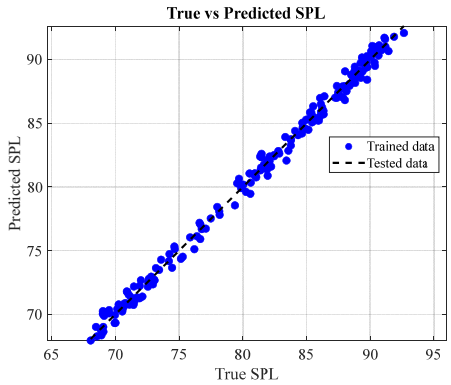

Fig. 12 The DNN-predicted SPL values against ground-truth simulation results for both training and test datasets

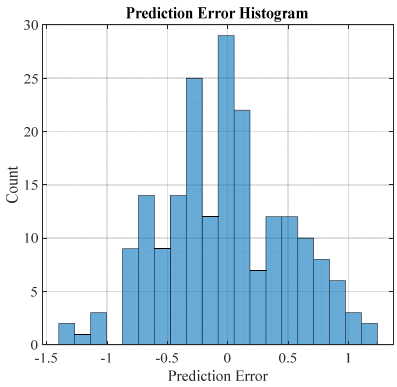

Fig. 13 The distribution of prediction errors (true SPL − predicted SPL) across the dataset

plotting training and validation loss across successive epochs. The training loss (blue) decreases monotonically, reflecting the model's ability to minimize error on the training dataset. The validation loss (orange) serves as a proxy for generalization performance, with divergence between the curves indicating overfitting. The convergence of both losses to a stable minimum (e.g., 0.02–0.04) suggests a well-trained model capable of accurate predictions. Discrepancies in the validation loss may necessitate adjustments such as dropout layers or early stopping. This plot is indispensable for diagnosing model behavior, ensuring robustness, and guiding hyperparameter tuning to balance bias and variance in the surrogate model.

Fig. 12 compares the DNN-predicted SPL values against ground-truth simulation results for both training and test datasets. Close alignment between the curves underscores the DNN's fidelity in approximating the complex relationship between input parameters and SPL. Minor deviations in the test data may highlight regions where the model lacks generalizability, potentially due to insufficient training samples or underrepresented parameter combinations. The plot validates the surrogate model's reliability for integration into the GA framework, ensuring that critical acoustic phenomena, such as resonance frequencies and damping effects, are accurately captured. Concrete systematic errors, if present, would necessitate model refinement or expanded training data.

Fig. 13 depicts the distribution of prediction errors (true SPL − predicted SPL) across the dataset. A symmetric, zero-centered distribution with narrow tails (e.g., errors within ±1.5 dB) indicates high precision and minimal bias. Skewness or outliers would suggest localized inaccuracies, potentially at specific frequencies or parameter ranges. This analysis is critical for identifying concrete systematic errors and guiding targeted improvements, such as architectural adjustments or enhanced sampling strategies. The histogram's shape also informs confidence intervals for predictions, which are vital for risk assessment in optimization tasks.

Fig. 14 provides a direct comparison of true and predicted SPL values for individual samples, indexed along the x-axis. Consistent overlap between the curves confirms

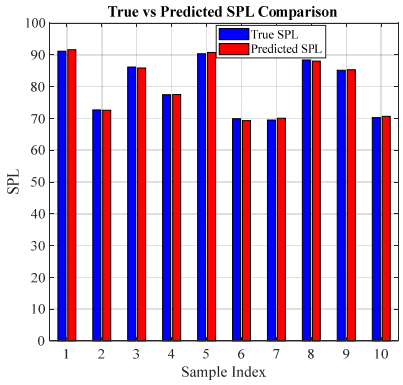

Fig. 14 A direct comparison of true and predicted SPL values for individual samples, indexed along the x-axis

the DNN's robustness across diverse parameter combinations. Discrepancies, particularly at resonance peaks, may indicate inadequate representation of high-SPL regions in the training data. Such visualizations are instrumental in pinpointing model weaknesses, facilitating iterative improvements, and ensuring comprehensive coverage of the design space. The plot also serves as a qualitative validation tool, complementing quantitative metrics like mean squared error.

The used hyperparameters of the DNN-GA algorithm is presented in Table 3.

Fig. 15 contrasts the SPL-frequency response of the GA-optimized design (using DNN predictions) with a baseline configuration. The optimized curve typically exhibits reduced peak SPL or shifted resonances, demonstrating the algorithm's efficacy in noise suppression. The y-axis (SPL in dB) and x-axis (frequency in Hz) highlight performance gains, with lower or smoother curves indicating superior acoustic performance. This visualization is pivotal for validating the DNN-GA framework's practical utility, showcasing its ability to derive designs that meet or exceed predefined acoustic targets. The plot also underscores the synergy between surrogate modeling and evolutionary optimization in complex engineering tasks.

Table 3 The used hyperparameters of the DNN-GA algorithm

Category	Hyperparameter	Value / Description
DNN	Number of hidden layers	2
	Neurons per layer	20
	Activation function	ReLU
	Learning rater	0.01
	Optimizer	Adam or SGD
	Epochs	50
	Mini-batch size	32
	Loss function	Mean Squared Error (MSE)
	Validation split	20% of training data
	Early stopping	Enabled (after certain validation stagnation)
GA	Population size	50 individuals
	Max generations	100
	Selection method	Roulette wheel
	Crossover Rater	0.8
	Mutation rate	0.05
	Elite count	2–5
	Crossover function	Arithmetic / Two-point crossover
	Mutation function	Uniform /
	Fitness function	1 / MSE or any other performance metric
	Termination criteria	Max generations or fitness tolerance
Dataset (Simulated)	Number of samples	200
	Input feature range	[0, 10]
	Output SPL range	[70–90] dB
Feature composition	Input features are composed of geometrical and physical parameters	
	Data generation strategy	Synthetic data generated by presented simulation
	Pre-processing steps	Data normalization to the range [0, 1], and feature scaling using MinMaxScaler

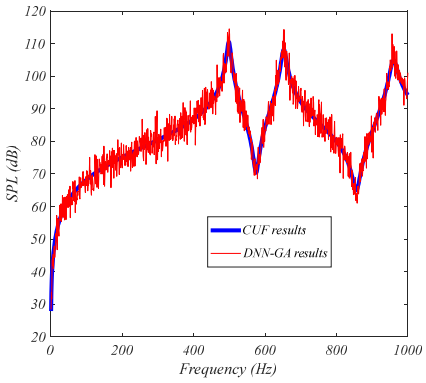

Fig. 15 The SPL-frequency response of the GA-optimized design with a baseline configuration

6. Conclusions

This study presented a comprehensive investigation into the stochastic vibro-acoustic behavior of FGP plates integrated with NCPSD, modeled through the refined CUF. By combining advanced shunt circuit configurations with a high-fidelity structural modeling approach, a robust and adaptive control strategy was developed for smart, lightweight structures operating under random and uncertain excitations. The CUF framework enabled accurate representation of electromechanical coupling by capturing transverse shear effects, thickness-wise material gradation, and multilayer interactions—capabilities that significantly outperform traditional modeling techniques, especially in the presence of complex boundary conditions and stochastic inputs. The inclusion of resistive-inductive-negative capacitance elements in the NCPSD architecture allowed for tunable broadband damping, leveraging the destabilizing feedback mechanism of negative capacitance to effectively suppress vibrations and radiated sound energy in mid- and high-frequency regimes. Crucially, the integration of a DNN-GA optimization strategy provided an intelligent layer to the control framework. The genetic algorithm component efficiently explored the hyperparameter space of the RL-NC circuits, while the deep neural network served as a surrogate

model to predict concrete system dynamics and optimize responses under varying environmental conditions. Numerical simulations confirmed the concrete system's effectiveness in mitigating both structural and acoustic responses, even under parameter uncertainties and stochastic disturbances. The DNN-GA-enhanced approach enabled real-time adaptation and optimization, reinforcing the concrete system's resilience and adaptability across a broad operational spectrum. Moreover, the synergy between functionally graded material tailoring, intelligent active shunting, and unified structural modeling laid the foundation for scalable, high-performance vibration and noise control in multifunctional applications. The findings underscore the transformative potential of combining physics-based formulations with data-driven optimization for the design of next-generation smart structures. Potential applications include aerospace, automotive, and precision engineering domains, where noise attenuation, dynamic reliability, and weight efficiency are critical. Future research directions include experimental validations, exploration of multi-physical coupling effects, and the further advancement of machine learning-enabled control strategies for complex and dynamic environments.

References

Al-Osta, M.A. (2022), "An exponential-trigonometric quasi-3d hsdt for wave propagation in an exponentially graded plate with microstructural defects", *Compos. Struct.*, **297**, p. 115984. https://doi.org/10.1016/j.compstruct.2022.115984

Barati, M., Sadr, M. and Zenkour, A. (2016), "Buckling analysis of higher order graded smart piezoelectric plates with porosities resting on elastic foundation", *Int. J. Mech. Sci.*, **117**, 309-320. https://doi.org/10.1016/j.ijmecsci.2016.09.012

Behjat, B., Salehi, M., Armin, A., Sadighi, M. and Abbasi, M. (2011), "Static and dynamic analysis of functionally graded piezoelectric plates under mechanical and electrical loading", *Scientia Iranica*, **18**(4), 986-994. https://doi.org/10.1016/j.scient.2011.07.009

Berardengo, M., Manzoni, S., Vanali, M. and Bonsignori, R. (2021), "Enhancement of the broadband vibration attenuation of a resistive piezoelectric shunt", *J. Intell. Mater. Syst. Struct.*, **32**(18-19), 2174-2189. https://doi.org/10.1177/1045389X20988090

Bodaghi, M. and Shakeri, M. (2012), "An analytical approach for free vibration and transient response of functionally graded piezoelectric cylindrical panels subjected to impulsive loads", *Compos. Struct.*, **94**(5), 1721-1735. https://doi.org/10.1016/j.compstruct.2012.01.009

Carrera, E. (1995), "A class of two-dimensional theories for anisotropic multilayered plates analysis", *Atti della accademia delle scienze di Torino. Classe di scienze fisiche matematiche e naturali*, **19**, 1-39. https://api.semanticscholar.org/CorpusID:115386465

Carrera, E. (1996), "C^0 reissner–mindlin multilayered plate elements including zig-zag and interlaminar stress continuity", *Int. J. Numer. Methods Eng.*, **39**(11), 1797-1820. https://doi.org/10.1002/(SICI)1097-0207(19960615)39:11<1797::AID-NME928>3.0.CO;2-W

Carrera, E. (1998), "Mixed layer-wise models for multilayered plates analysis", *Compos. Struct.*, **43**(1), 57-70. https://doi.org/10.1016/S0263-8223(98)00097-X

Carrera, E. (2001), "Developments, ideas, and evaluations based upon reissner's mixed variational theorem in the modeling of multilayered plates and shells", *Appl. Mech. Rev.*, **54**(4), 301-329. https://doi.org/10.1115/1.1385512

Carrera, E. (2003), "Theories and finite elements for multilayered plates and shells: a unified compact formulation with numerical assessment and benchmarking", *Arch. Computat. Methods Eng.*, **10**, 215-296. https://doi.org/10.1007/BF02736224

Carrera, E. (2005), "Transverse normal strain effect on thermal stress analysis of homogeneous and layered plates", *AIAA J.*, **43**(10), 2232-2242. https://doi.org/10.2514/1.11230

Carrera, E. and Kröplin, B. (1997), "Zigzag and interlaminar equilibria effects in large-deflection and postbuckling analysis of multilayered plates", *Mech. Compos. Mater. Struct.. Int. J.*, **4**(1), 69-94. https://doi.org/10.1080/10759419708945875

Carrera, E. and Pagani, A. (2014), "Free vibration analysis of civil engineering structures by component-wise models", *J. Sound Vib.*, **333**(19), 4597-4620. https://doi.org/10.1016/j.jsv.2014.04.063

Carrera, E. and Zozulya, V. (2024), "Carrera unified formulation (cuf) for the composite plates and shells of revolution. layer-wise models", *Compos. Struct.*, **334**, p. 117936. https://doi.org/10.1016/j.compstruct.2024.117936

Chen, J., Zhang, W., Xiao, J., Jiang, T. and Chang, J. (2025), "Electro-mechanical analysis of piezoelectric sandwich structure", *Mech. Adv. Mater. Struct.*, **32**(4), 730-748. https://doi.org/10.1080/15376494.2024.2355368

Ebrahimi, F., Barati, M.R. and Dabbagh, A. (2016), "A nonlocal strain gradient theory for wave propagation analysis in temperature-dependent inhomogeneous nanoplates", *Int. J. Eng. Sci.*, **107**, 169-182. https://doi.org/10.1016/j.ijengsci.2016.07.008

Ebrahimi, F., Barati, M.R. and Haghi, P. (2017), "Thermal effects on wave propagation characteristics of rotating strain gradient temperature-dependent functionally graded nanoscale beams", *J. Thermal Stress.*, **40**(5), 535-547. https://doi.org/10.1080/01495739.2016.1230483

Eyvazian, A., Zhang, C., Civalek, Ö., Khan, A., Sebaey, T.A. and Farouk, N. (2022), "Wave propagation analysis of sandwich fgm nanoplate surrounded by viscoelastic foundation", *Arch. Civil Mech. Eng.*, **22**(4), p. 159. https://doi.org/10.1007/s43452-022-00474-w

Fahy, F.J. (2007), *Sound and structural vibration: radiation, transmission and response*, Elsevier. https://books.google.com/books?id=caelfFmWC28C

Fourn, H., Atmane, H.A., Bourada, M., Bousahla, A.A., Tounsi, A. and Mahmoud, S.R. (2018), "A novel four variable refined plate theory for wave propagation in functionally graded material plates", *Steel Compos. Struct., Int. J.*, **27**(1), 109-122. https://doi.org/10.12989/scs.2018.27.1.109

Gao, J., Zhao, P., Zhang, X., Shi, W., Sun, Y., Lan, X., Liu, Y. and Leng, J. (2025), "Active vibration control of high-stiffness heavy cantilever beam based on piezoelectric stack actuators", *Mech. Adv. Mater. Struct.*, 1-15. https://doi.org/10.1080/15376494.2025.2468375

Gozum, M.M., Aghakhani, A., Serhat, G. and Basdogan, I. (2018), "Electroelastic modeling of thin-laminated composite plates with surface-bonded piezo-patches using rayleigh–ritz method", *J. Intell. Mater. Syst. Struct.*, **29**(10), 2192-2205. https://doi.org/10.1177/1045389X18758189

Guo, L., Xin, X., Shahsavari, D. and Karami, B. (2022), "Dynamic response of porous e-fgm thick microplate resting on elastic foundation subjected to moving load with acceleration", *Thin-Wall. Struct.*, **173**, p. 108981. https://doi.org/10.1016/j.tws.2022.108981

Gupta, V., Barak, M. and Das, S. (2023), "Vibrational analysis of size-dependent thermo-piezo-photo-electric semiconductor medium under memory-dependent moore–gibson–thompson

photo-thermoelasticity theory", *Mech. Adv. Mater. Struct*., 1-17. https://doi.org/10.1080/15376494.2023.2291804

Kurt, P., Narayan, B., Roscow, J.I. and Orhan, S. (2024), "Improving piezoelectric energy harvesting performance through mechanical stiffness matching", *Mech. Adv. Mater. Struct*., **31**(28), 10721-10734. https://doi.org/10.1080/15376494.2023.2295383

Li, F.L., Wang, C.N. and Hao, Y.X. (2024), "Free vibration and sound radiation of abh-type functionally graded sandwich plates under elastic boundary restraints", *Mech. Adv. Mater. Struct*., **31**(28), 10367-10381. https://doi.org/10.1080/15376494.2023.2289054

Liu, F., Shi, P., Shen, Y., Xu, Y. and Yang, Z. (2024), "Advances in suppression of structural vibration and sound radiation by flexural wave manipulation", *Thin-Wall. Struc*., **200**, p. 111936. https://doi.org/10.1016/j.tws.2024.111936

Long, S.X., Khoo, S.Y., Ong, Z.C., Soong, M.F., Huang, Y.H., Prasath, N. and Noroozi, S. (2024), "A comprehensive review on mechanical amplifier structures in piezoelectric energy harvesters", *Mech. Adv. Mater. Struct*., **31**(25), 7244-7273. https://doi.org/10.1080/15376494.2023.2243674

Moradi-Dastjerdi, R. and Behdinan, K. (2021), "Stress waves in thick porous graphene-reinforced cylinders under thermal gradient environments", *Aerosp. Sci. Technol*., **110**, p. 106476. https://doi.org/10.1016/j.ast.2020.106476

Najd, J., Zappino, E., Carrera, E., Harizi, W. and Aboura, Z. (2024), "Optimal position and dimensions of embedded normal piezoelectric transducers, higher order plate models and experimental approach", *Mech. Adv. Mater. Struct*., 1-12. https://doi.org/10.1080/15376494.2024.2342028

Patil, H.H. and Pitchaimani, J. (2024), "Sound radiation characteristics of a beam under supersonic airflow and non-uniform temperature field", *Aerosp. Sci. Technol*., **147**, p. 109001. https://doi.org/10.1016/j.ast.2024.109001

Quan, T.Q. and Dinh Duc, N. (2016), "Nonlinear vibration and dynamic response of shear deformable imperfect functionally graded double-curved shallow shells resting on elastic foundations in thermal environments", *J. Thermal Stress*., **39**(4), 437-459. https://doi.org/10.1080/01495739.2016.1158601

Ramirez, F., Heyliger, P.R. and Pan, E. (2006), "Free vibration response of two-dimensional magneto-electro-elastic laminated plates", *J. Sound Vib*., **292**(3-5), 626-644. https://doi.org/10.1016/j.jsv.2005.08.004

Ravanbod, M. and Ebrahimi-Nejad, S. (2024), "Perforated auxetic honeycomb booster with reentrant chirality: a new design for high-efficiency piezoelectric energy harvesting", *Mech. Adv. Mater. Struct*., **31**(27), 9857-9872. https://doi.org/10.1080/15376494.2023.2280997

Reddy, J.N. (2003), *Mechanics of laminated composite plates and shells: theory and analysis*, CRC press. https://doi.org/10.1201/b12409

Reddy, R.K.K., Veerappan, A., George, N. and Bhagat, V. (2024), "Thermo-mechanical buckling and sound radiation characteristics of 3d graphene porous core curved sandwich panels with composite facings", *Thin-Wall. Struct*., **199**, p. 111753. https://doi.org/10.1016/j.tws.2024.111753

Robaldo, A., Carrera, E. and Benjeddou, A. (2006a), "A unified formulation for finite element analysis of piezoelectric adaptive plates", *Comput. Struct*., **84**(22-23), 1494-1505. https://doi.org/10.1016/j.compstruc.2006.01.029

Robaldo, A., Carrera, E. and Benjeddou, A. (2006b), "A unified formulation for finite element analysis of piezoelectric adaptive plates", *Comput. Struct*., **84**(22-23), 1494-1505. https://doi.org/10.1016/j.compstruc.2006.01.029

Sha, L., Sun, H., Wang, Y. and Zhou, L. (2024), "Electro-mechanical coupling enriched finite element method for dynamic characteristic of piezoelectric materials structures", *Mech. Adv. Mater. Struct*., **31**(25), 6803-6816. https://doi.org/10.1080/15376494.2023.2238212

Vel, S.S., Mewer, R. and Batra, R. (2004), "Analytical solution for the cylindrical bending vibration of piezoelectric composite plates", *Int. J. Solids Struct*., **41**(5-6), 1625-1643. https://doi.org/10.1016/j.ijsolstr.2003.10.012

Wei, P.F., He, M.X. and Ding, Q. (2024), "Vibration and sound radiation of acoustic black hole beams on pasternak foundation by the riccati transfer matrix method", *Appl. Acoust*., **217**, p. 109840. https://doi.org/10.1016/j.apacoust.2023.109840

Wu, S.Y. (1996), "Piezoelectric shunts with a parallel RL circuit for structural damping and vibration control", Presented at the Smart Structures and Materials 1996: Passive Damping and Isolation, Spie, Vol. 2720, pp. 259-269. https://doi.org/10.1117/12.239093

Yang, J. (2010), *Special topics in the theory of piezoelectricity*, Springer Science & Business Media. https://doi.org/10.1007/978-0-387-89498-0

Yang, W., Chang, L., Alnowibet, K.A. and El-Meligy, M. (2024), "Enhancing the efficiency and energy capacity of the tri-directional fg nanoplate attached to the piezoelectric patch validated by artificial intelligence", *Aerosp. Sci. Technol*., **155**, p. 109694. https://doi.org/10.1016/j.ast.2024.109694

Zhang, Q., Xie, M., Zhou, D., Habibi, M. and Khorami, M. (2024), "Bending responses of graphene nanoplatelets reinforced sandwich cylindrical micro panel with piezoelectric layers", *Mech. Adv. Mater. Struct*., 1-16. https://doi.org/10.1080/15376494.2024.2385008

Zhao, Y., Dai, W., Wang, Z. and Ragab, A.E. (2024), "Application of computer simulation to model transient vibration responses of gpls reinforced doubly curved concrete panel under instantaneous heating", *Mater. Today Commun*., **38**, p. 107949. https://doi.org/10.1016/j.mtcomm.2023.107949